

# Intrinsic control of interlayer exciton generation rate in van der Waals materials via Janus layers

Engin Torun,<sup>\*,†,||</sup> Fulvio Paleari,<sup>\*,‡,||</sup> Milorad V. Milošević,<sup>¶</sup> Ludger Wirtz,<sup>†</sup> and  
Cem Sevik<sup>\*,§,¶</sup>

<sup>†</sup>*Department of Physics and Materials Science, University of Luxembourg, 162a avenue de la Faiënerie, L-1511 Luxembourg, Luxembourg*

<sup>‡</sup>*CNR-NANO, Via Campi 213a, 41125 Modena, Italy*

<sup>¶</sup>*Department of Physics & NANOLab Center of Excellence, University of Antwerp, Groenenborgerlaan 171, B-2020 Antwerp, Belgium*

<sup>§</sup>*Department of Mechanical Engineering, Faculty of Engineering, Eskisehir Technical University, 26555 Eskisehir, Turkey*

*|| Contributed equally to this work*

E-mail: engntr@gmail.com; fulvio.paleari@nano.cnr.it; csevik@eskisehir.edu.tr

## Abstract

We demonstrate the possibility of engineering the optical properties of transition metal dichalcogenide heterobilayers when one of the constitutive layers has a Janus structure. This has important consequences for the charge separation efficiency. We investigate different MoS<sub>2</sub>@Janus layer combinations using first-principles methods including electron-hole interactions (excitons) and exciton-phonon coupling. The direction of the intrinsic electric field from the Janus layer modifies the electronic band alignments and, consequently, the energy separation between interlayer exciton states – which usually have a very low oscillator strength and hence are almost dark in absorption – and bright in-plane excitons. We find that in-plane lattice vibrations strongly

couple the two states, so that exciton-phonon scattering may be a viable generation mechanism for interlayer excitons upon light absorption. In particular, in the case of MoS<sub>2</sub>@WSSe, the energy separation of the low-lying interlayer exciton from the in-plane exciton is resonant with the transverse optical phonon modes (40 meV). We thus identify this heterobilayer as a prime candidate for efficient electron-hole pair generation with efficient charge carrier separation.

## Introduction

The weak dielectric screening of two-dimensional semiconductors allows for the formation of strongly bound electron-hole pairs (excitons) upon light absorption, leading to peculiar optical properties such as discrete excitonic peaks with strong photoluminescence response and layer-dependent exciton modulation<sup>1-4</sup>. In this regard, two-dimensional transition metal dichalcogenides (TMDs) are exemplary since, due to the quasi 2D confinement and weak dielectric screening, they host excitons with binding energies of hundreds of meV<sup>5-8</sup>. Therefore, this class of materials represents an important testbed for the physics of light-matter interaction<sup>8</sup>, as evidenced by a wealth of observed phenomena including exciton/polariton condensation<sup>9-11</sup>, the realization of advanced optoelectronic and nanophotonic devices<sup>12-16</sup>, as well as valleytronics.<sup>17,18</sup>

Peculiarly, heterobilayer (HBL) structures with different TMD layers generally host interlayer (IL) excitons (where electron and hole forming the exciton reside in different layers) with a static electric dipole moment. Earlier reports showed that the type-II band alignment of the constituent monolayers causes the IL exciton to be the lowest-energy excitation in the HBL absorption spectrum despite having smaller binding energy than in-plane (IP) excitons<sup>19-23</sup>. These IL excitons have a lifetime almost 100 times longer than the more commonly observed in-plane (intralayer – IP) excitons — where electron and hole reside in the same layer<sup>24,25</sup> — and are also at the forefront of current research. For example, their ultrafast formation dynamics is investigated<sup>26,27</sup>, along with their role in valleytronics<sup>28,29</sup> and charge

transfer.

Ovesen *et al.*<sup>30</sup> have suggested a scenario for the formation of the IL excitons in HBL TMDs: the excitation of the IP exciton due to light absorption is followed by the tunneling of holes into a finite-momentum state of the opposite layer which can then relax to the ground state of the IL exciton via phonon-scattering. Therefore, the energy-momentum dependence and exciton energy offsets in bilayer structures are crucial for the formation of IL excitons in HBLs. These excited-state features also strongly depend on structural degrees of freedom such as layer separation and stacking. By these means the engineering of optical transition strengths, energies, and selection rules have been previously demonstrated<sup>31–35</sup>, notably by the application of external electric fields<sup>21,36–38</sup>.

However, the electric field does not need to be external: the addition of a so-called “Janus” layer<sup>39</sup> can provide a strong intrinsic electric field. Janus monolayers have been demonstrated by experimental studies. Qin *et al.*<sup>40</sup> have recently reported an *in situ* growth process which results in Janus TMD monolayers with high structural and optical quality. A first theoretical prediction of the impact of the intrinsic electric field, with a possible reordering of IP and IL excitons, was done recently for Janus-bilayers<sup>41</sup>. In this paper, we propose that combining a non-Janus TMD monolayer with a Janus monolayer – thus creating a TMD@JTMD heterostructure – allows for reliable tuning of the relative order of the IP and IL excitons, in turn leading to an efficient pathway for IP-to-IL conversion via exciton-phonon scattering. Experimentally, Trivedi *et al.*<sup>42</sup> have already shown the controllable room temperature fabrication and optical characterization of TMD@JTMD and JTMD@JTMD HBL crystals. The tuning of the intrinsic net out-of-plane electric dipole moment in these materials, with the large corresponding piezoelectric effect<sup>39</sup>, is also promising for light-energy/electricity interconversions and valley-contrasting physics<sup>43–46</sup>.

More specifically, we investigate the optoelectronic properties of MoS<sub>2</sub>@MoSSe, MoS<sub>2</sub>@MoSeS, MoS<sub>2</sub>@WSSe, and MoS<sub>2</sub>@WSeS (as shown in Fig. 1a-d) using first-principles, many-body perturbation theory techniques including quasiparticle corrections, electron-hole interactions

and exciton-phonon coupling<sup>47–54</sup>. We demonstrate that the direction of the intrinsic electric field polarization of the Janus layer changes both the band alignments and the energy separation of the lowest-energy IL and IP excitonic levels. In addition, we calculate the scattering strength of the IP-to-IL exciton transitions mediated by optical phonons at the zone center, in order to address the generation mechanisms of the charge-separated and long-lived IL excitons as schematically explained in Fig. 1e.

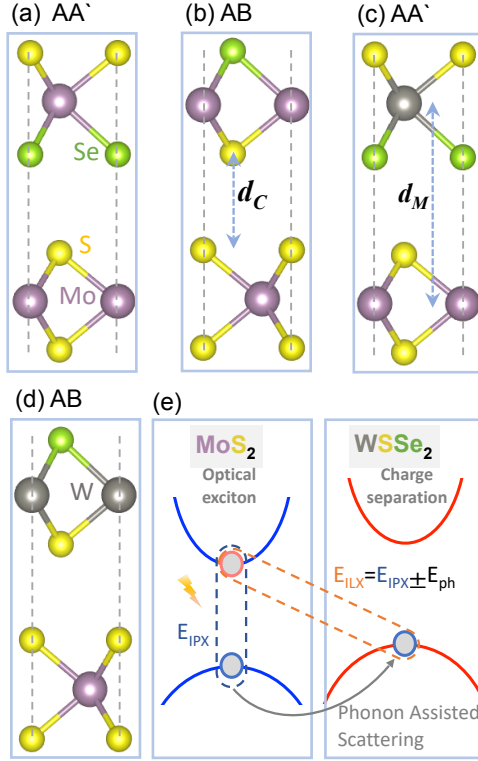


Figure 1: (a) to (d): Schematic representation of the investigated TMD@JTMD heterobilayer structures (only the most stable configurations are reported). The TMD layer (bottom) is always MoS<sub>2</sub>. The JTMD layer (top) is either MoS<sub>2</sub>Se or WSe<sub>2</sub>, while the TMD@JTMD interface can be either S-S or S-Se. Moreover, the two layers can be stacked in different configurations denoted AA' and AB. (e): Schematic representation of the phonon-assisted IP  $\rightarrow$  IL exciton transition in the case of MoS<sub>2</sub>@WSe<sub>2</sub>.

# Results and discussion

## Structural properties and stability with respect to stacking order and Janus layer polarization

Table 1: The calculated lattice constants ( $a_0$ ), interlayer separation of metal ( $d_M$ ) and chalcogen ( $d_C$ ) atoms, total energy with respect to minimum energy stacking ( $E_{tot}$ ), electronic direct/indirect band gap at PBE ( $E_{gap}^{DFT}$ ) and  $G_0W_0$  level ( $E_{gap}^{GW}$ ), inter-layer (IL) and in-plane (IP) exciton energies of the HBLs.

HLB	ST	$a_0$ (Å)	$d_M/d_C$ (Å)	$E_{tot}$ (meV/atom)	$E_{gap}^{DFT}$ dir./ind. (eV)	$E_{gap}^{GW}$ dir./ind. (eV)	<b>IL</b> (eV)	<b>IP</b> (eV)
MoS <sub>2</sub> @MoSeS	AB	3.22	6.33/3.14	0.14	0.87/0.82	1.85/1.82		
	AA	3.22	7.01/3.75	11.48	0.80/0.90	1.79/1.89		
	<b>AA'</b>	<b>3.22</b>	<b>6.41/3.15</b>	<b>0.00</b>	<b>0.83/0.81</b>	<b>1.80/1.81</b>	<b>1.38</b>	<b>1.82</b>
MoS <sub>2</sub> @MoSSe	<b>AB</b>	<b>3.23</b>	<b>6.15/3.06</b>	<b>0.00</b>	<b>1.44/0.93</b>	<b>2.44/1.84</b>	<b>1.90</b>	<b>1.83</b>
	AA	3.22	6.79/3.70	9.65	1.35/1.14	2.38/2.08		
	AA'	3.22	6.18/3.10	0.19	1.39/0.94	2.39/1.84		
MoS <sub>2</sub> @WSeS	AB	3.22	6.35/3.09	0.19	0.55/0.67	1.62/1.71		
	AA	3.22	6.97/3.70	13.79	0.46/0.73	1.55/1.75		
	<b>AA'</b>	<b>3.22</b>	<b>6.37/3.10</b>	<b>0.00</b>	<b>0.51/0.65</b>	<b>1.57/1.69</b>	<b>1.15</b>	<b>1.83</b>
MoS <sub>2</sub> @WSSe	<b>AB</b>	<b>3.22</b>	<b>6.08/3.00</b>	<b>0.00</b>	<b>1.12/0.82</b>	<b>2.20/1.81</b>	<b>1.78</b>	<b>1.83</b>
	AA	3.22	6.73/3.64	12.61	1.00/1.04	2.11/2.03		
	AA'	3.22	6.12/3.03	0.29	1.06/0.83	2.14/1.82		

The calculated results for the geometric and electronic properties are reported in Table 1. The obtained in-plane lattice parameters are in excellent agreement with the reported values<sup>55,56</sup> and do not depend on the stacking order. However, the out-of-plane structural parameters  $d_C$  (interlayer distance between closest chalcogen layers) and  $d_M$  (interlayer distance between metal atom layers) change with the stacking type. These stacking-dependent structural changes do not remarkably affect electronic structures, as seen in the calculated band gaps and exciton energies also reported in Table 1. Among all the considered systems (see Supplementary Information<sup>57</sup> for more details), the difference in total energies between the various structures is of the order of a few meV, with the so-called AA-stacked structures clearly being less energetically favored due to the in-line chalcogen-chalcogen interlayer interaction. Therefore, within the limit of computational error, either the AB or AA' stackings can lead to stable structures depending on the orientation of the Janus layer.

At variance with the stacking order, the polarization direction of the Janus layer (namely S-Mo-S $\leftrightarrow$ S-Metal-Se or S-Mo-S $\leftrightarrow$ Se-Metal-S, with a different interaction at the layers interface) has a notable effect on both structural and electronic properties. In particular, the energy difference between direct and indirect band gaps, as well as the exciton binding energies, change remarkably. For instance, MoS<sub>2</sub>@MoSSe(WSSe) HBLs are distinctly indirect band gap materials, whereas MoS<sub>2</sub>@MoSeS(WSSe) are direct band gap materials within the limits of thermal fluctuations.

## Excitonic properties

The results for quasiparticle band structures (in the  $G_0W_0$  approximation) and the absorption spectra including electron-hole interactions for AA' and AB stacked HBLs are displayed in Fig. 2(a-d) (left: excitonic optical absorption spectrum; right: quasiparticle band structure in the vicinity of the  $K$  point of the hexagonal Brillouin zone (BZ); see Supplementary Information<sup>57</sup> for all the considered materials). The band structures include the projections of the electronic wave functions onto atomic orbitals localized on the constituent layers: the red and blue colors represent electronic states mostly localized on the Janus and on the TMD monolayer, respectively. Electron-hole interactions were included via the solution of the Bethe-Salpeter equation (BSE) from first principles.<sup>58</sup>

The investigated structures differ in stacking geometry (AA' vs AB), transition metal in the Janus layer (Mo vs W) and orientation of the Janus layer, controlling the polarization direction (S $\leftrightarrow$ S vs S $\leftrightarrow$ Se interface between the two layers). All the HBLs present some common optoelectronic features, as well as some notable differences. The electronic states around the  $K$  points in the quasiparticle band structures are completely confined on one of the two layers. In particular, the four highest valence states comprise two pairs of spin-orbit-split bands, with one pair localised on the TMD layer (blue color) and the other pair on the Janus layer (red color). The same is true for the four lowest conduction states. In addition,

the minimum energy transition at the  $K$  point always connects a valence state on the Janus layer to a conduction state on the TMD one. As a consequence of the band structure shape, the low-energy region of the excitonic absorption spectra is always dominated by the IP and IL excitons originated from single-particle transitions in the bands around  $K$ . Another common excitonic feature is that the low-lying IP states always originate from electronic transition between the TMD valence and conduction bands (blue to blue in the band graph), therefore they are always localised on the TMD layer, as shown in two examples in Fig. 2e-g.

The four HBLs however differ remarkably with respect to the nature of the quasiparticle band gap, which is direct at  $K$  for the AA' stackings with S-Se interface (Fig. 2(a) and (c)), while indirect from  $\Gamma$  to  $K$  for the AB stackings with S-S interface (Fig. 2(b) and (d)). Another important difference is due to the effect of the intrinsic electric field arising from the Janus monolayer, which shifts the TMD bands with respect to the Janus ones in both valence and conduction states. The direction of the shift depends on the direction of the field, i.e., on the orientation of the Janus layer. More specifically, in the HBLs with S/Se interface the TMD bands are shifted *away* from the Janus ones, leading to a substantial energy separation. When the Janus dipole orientation is reversed, instead, the TMD bands are shifted *closer* to the Janus ones becoming almost degenerate with them. These changes at the quasiparticle level determine the most important optical feature for charge transfer efficiency: the energy difference – and thus likelihood of transition – between the IL and IP excitonic states, which varies considerably between the systems. Intriguingly, the localization of the IL excitons changes depending on the stacking and JTMD layer types. In  $\text{MoS}_2@ \text{MoSSe}$ , the exciton is formed by electronic transitions from the TMD layer to the JTMD one (blue to red in the band graph), while in all other cases the hole is on the JTMD layer and the electron on the TMD one (red to blue in the band graph). This difference in spatial localization can be seen in Fig. 2f-g.

*MoS<sub>2</sub>@MoSeS (AA' stacking, S-Se interface).* The geometry of this system is represented in Fig. 1(a), the quasiparticle/BSE results in Fig. 2(a). This HBL is a direct gap material

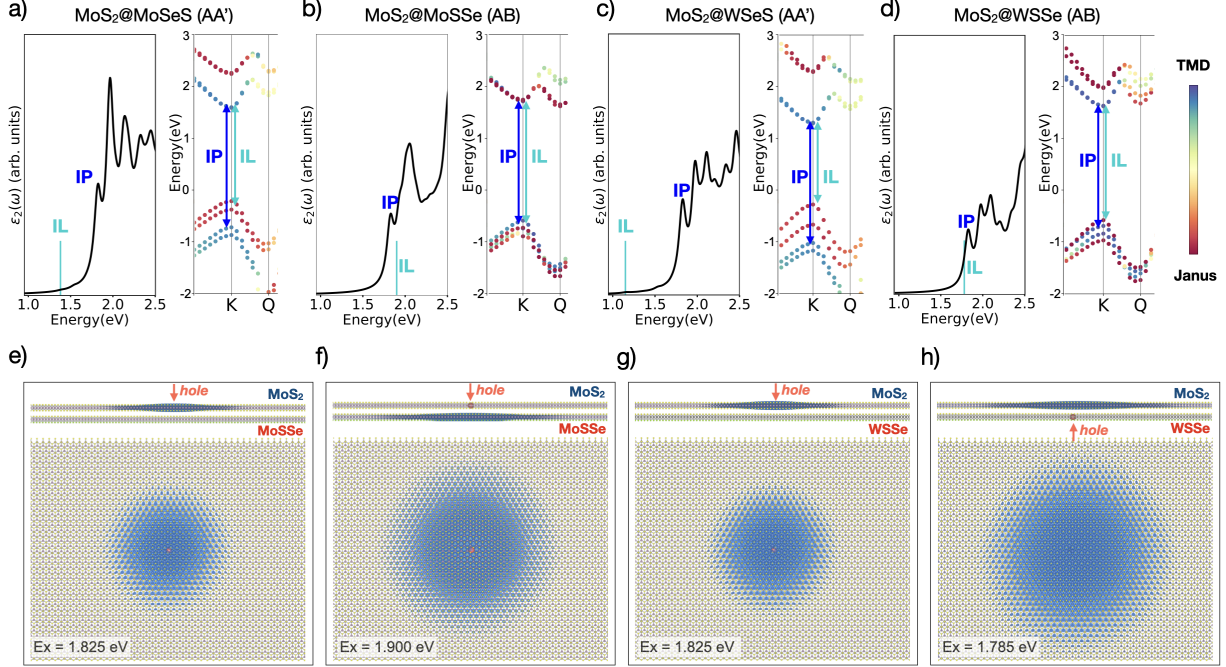


Figure 2: Excitonic properties of TMD@JTMD HBLs. Top panels (a to d): optical absorption spectra and quasiparticle band structures (zoomed-in to the vicinity of the  $K$  point in the BZ, see the supplementary materials for the full band structures) of the investigated systems. The absorption spectrum is proportional to the imaginary part of the excitonic dielectric function  $\epsilon_2$ , which is the plotted quantity on the left panels. The band color (right panels) represents the projections of the electronic wave function onto its atomic orbitals localized either in the JTMD or in the TMD layers (blue: mostly TMD state, red: mostly Janus state). The calculations are performed on the stacking configurations with minimal energy and are: (a) MoS<sub>2</sub>@MoSeS in AA' stacking, (b) MoS<sub>2</sub>@MoSSe in AB stacking, (c) MoS<sub>2</sub>@WSeS in AA' stacking and (d) MoS<sub>2</sub>@WSSe in AB stacking. The most important single-particle transitions forming the IL (Janus  $\leftrightarrow$  MoS<sub>2</sub>), IP (MoS<sub>2</sub>  $\leftrightarrow$  MoS<sub>2</sub>) excitons are labeled in the band plots, while the energy of the resulting exciton states is emphasized in the absorption plots. Bottom panels (e to h): Wave-function intensity plot in real space for excitons corresponding to (e) IP in MoS<sub>2</sub>@MoSSe, (f) IL in MoS<sub>2</sub>@MoSSe, (g) IP in MoS<sub>2</sub>@WSSe, and (h) IL in MoS<sub>2</sub>@WSSe. The plot is obtained by fixing the hole in a position consistent with its band orbital character and plotting the resulting electron distribution.

with a gap of 1.80 eV. The indirect band gap sits 0.01 eV above. Note that at the DFT-PBE level this energy ordering is reversed as seen in Table 1, which shows that the quasiparticle correction to the Kohn-Sham energies is not just a rigid shift of the bands owing to the  $k$ -dependence of the  $GW$  self-energy. The ordering of the bands at the  $K$  point indicates a type-II character for this HBL at the quasiparticle level, as previously observed for MoS<sub>2</sub>@WS<sub>2</sub> and



MoSe<sub>2</sub>@WSe<sub>2</sub> HBLs.<sup>19,20,22,23</sup> The energy of the IL exciton which forms via the transitions from the valence band maximum (VBM) to conduction band minimum (CBM) is 1.38 eV. The energy difference between the lowest energy IL and the first in-plane exciton, IP, is 0.44 eV, which is too large for a one-phonon scattering process to enable the direct transitions from the optically excited IP to the IL state.

*MoS<sub>2</sub>@MoSSe (AB stacking, S-S interface).* The geometry of this system is represented in Fig. 1(b) and the quasiparticle/BSE results are shown in Fig. 2(b). Contrary to the previous case, here we have an indirect gap semiconductor at both the DFT-PBE (0.93 eV) and G<sub>0</sub>W<sub>0</sub> (1.84 eV), respectively. Because of the direction of the intrinsic electric field, the TMD and Janus bands overlap at the CBM and have very similar band energies at the VBM. This leads to a situation where the electron-hole interaction strength of the IL and IP excitons become the determining factor for the energy ordering of these excitons in the absorption spectrum. In MoS<sub>2</sub>@WS<sub>2</sub> and MoSe<sub>2</sub>@WSe<sub>2</sub> HBLs it has been shown that the binding energies<sup>1</sup> of IL excitons are approximately 100 meV lower than the ones of IP excitons<sup>22</sup>. The case of the MoS<sub>2</sub>@MoSSe HBL, here, is similar: the IP exciton (1.83 eV) has approximately 70 meV higher binding energy than the first IL exciton (1.90 eV) as reported in Table 1. Due to this, the IP exciton automatically becomes the lowest energy exciton in the absorption spectrum as shown in Fig. 1(b). The spatial distribution of the excitonic wave functions for this system is shown in Fig. 2e and f for the IP and IL states, respectively. The energy separation between the IP and the IL exciton is around 70 meV. This is not ideal because the charge-separated state is not energetically favored, and even a thermal population of the IL exciton would be very tiny.

*MoS<sub>2</sub>@WSeS (AA' stacking, S-Se interface).* The geometry of this system is represented in Fig. 1(c) and the quasiparticle/BSE results are shown in Fig. 2(c). Similar to the Mo case, this is a direct band gap material with a quasiparticle gap of 1.57 eV (see Table1). Again, orbital projections indicate the type-II character of the electronic bands in this HBL.

---

<sup>1</sup>Here, the binding energy of an IP (IL) exciton is defined as the difference between the exciton energy and the lowest-energy single-particle IP (IL) transition.

The SOC splitting of the Janus bands, shown in red, is more pronounced than in the Mo case due to the presence of the heavier W atoms. Here the energy difference between the IL exciton (1.15 eV) and the lowest-energy IP exciton (1.83 eV) is 0.65 eV, even larger than in the Mo case with the same stacking and Janus orientation, due to the more substantial SOC. This again rules out efficient IL exciton generation from the IP states via first-order phonon-assisted conversion processes, with incoherent exciton scattering (i.e., relaxation dynamics<sup>30,59</sup>) likely being the most important mechanism.

*MoS<sub>2</sub>@WSSe (AB stacking, S-S interface).* The geometry of this system is represented in Fig. 1(d) and the quasiparticle/BSE results are shown in Fig. 2(d). This HBL has an indirect quasiparticle band gap of 1.81 eV. At the VBM, the TMD bands (blue) are squeezed in between SOC-split Janus bands (red). Compared to the previous W-based HBL, the opposite intrinsic dipole moment from the Janus layer shifts the bands of the MoS<sub>2</sub> layer so that the bands localized on the two layers are energetically very close to each other just as in the case of the Mo-based system with the same geometry. The lowest-lying IL state (1.78 eV) is just 40 meV below the IP exciton as shown in Fig. 2(d), while the real-space excitonic wavefunctions are represented in Fig. 2g-h. We will see in the following section that this small energy difference will drastically improve the efficiency of the exciton-phonon scattering channel between the two excitonic states and, hence, the charge carrier separation efficiency of this HBL.

## Exciton-phonon coupling strengths

We now focus on MoS<sub>2</sub>@WSSe (AB stacking), the HBL where the lowest-bound intralayer and interlayer excitons have a very small energy separation (40 meV), lower than the Debye energy (56 meV). This means that phonon-mediated charge separation, i.e., excitonic intralayer-interlayer (IP-IL) scattering might be very efficient, due to two concurring mechanisms. First, the exciton relaxation dynamics suggests that after the higher-energy in-

tralayer exciton is photoexcited, incoherent scatterings mediated by low-momentum acoustic phonons will quickly transfer the carriers to the lower-energy interlayer state (the description of out-of-equilibrium carrier dynamics is beyond the scope of this paper). Second, direct intralayer-interlayer scatterings mediated by optical phonons at vanishing momenta will also be permitted and may play an important role. We quantitatively analyze the latter mechanism by computing the exciton-phonon coupling matrix elements  $\mathcal{G}$  at zero exciton and phonon momenta for this system<sup>54,60–62</sup>:

$$\mathcal{G}_{\alpha\beta}^{\mu} = \sum_{vck} \left[ \sum_{v'} \left( A_{\beta}^{cv'k} \right)^* g_{vv'k}^{\mu} A_{\alpha}^{cvk} - \sum_{c'} \left( A_{\beta}^{c'vk} \right)^* g_{c'ck}^{\mu} A_{\alpha}^{cvk} \right] \quad (1)$$

Here we assume that excitons can be approximately described as well-defined quasiparticle excitations with bosonic character.<sup>63</sup> In Eq. (1),  $\alpha$  and  $\beta$  are the indices of the exciton states involved in a scattering mediated by a phonon mode  $\mu$ . The exciton eigenvectors  $A^{cvk}$  are expressed in terms of single-particle transitions at wave vector  $k$  from a valence band  $v$  to a conduction band state  $c$ . They represent the excitonic wave function and result from the solution of the BSE. The  $g_{c'ck}^{\mu}$  ( $g_{vv'k}^{\mu}$ ) are the *electron*-phonon coupling matrix elements, obtained from a density functional perturbation theory (DFPT) calculation and representing the scattering amplitude from a conduction band state  $c$  (valence band state  $v'$ ) at wave-vector  $k$  into another state  $c'$  ( $v$ ) at the same wave vector, via absorption/emission of a phonon mode  $\mu$ . Thus, the values of  $|\mathcal{G}_{\alpha\beta}^{\mu}|$  represent the coupling strengths of excitonic transitions  $\alpha \rightarrow \beta$  via absorption/emission of phonon mode  $\mu$ . The calculated values for the IL-IP scattering are displayed in Fig. 3a, showing that out of the 10 distinct optical phonon modes present in these material, all those with atoms oscillating in the layer plane may couple the two excitons and represent possible scattering channels. These are doubly degenerate modes with  $E$  symmetry. The coupling is instead forbidden for the out-of-plane phonons. This confirms that an IP exciton localised on one layer may transfer its carriers to the lower-lying IL one with the help of ionic oscillations in that layer. In the case of MoS<sub>2</sub>@WSSe,

the coupling strengths vary between 0.5 and 2 meV. A scheme of the oscillation patterns<sup>64</sup> is provided in Fig. 3b.

The other factor affecting scattering probabilities is energy conservation. We define the resonance offset energy (ROE) as  $\Delta E_{\alpha,\beta}^{\mu} = |E_{\alpha} - E_{\mu} - E_{\beta}|$  ( $E_{\mu}$  being the phonon energy). The closer  $\Delta E_{\alpha,\beta}^{\mu}$  is to zero, the more likely the transition is to happen. Here we consider only the phonon emission case, since it is the dominant contribution with respect to phonon absorption. The ROE values are shown with a color scale in Fig. 3a. For MoS<sub>2</sub>@WSSe, the energy of the fourth  $E$  phonon mode is exactly resonant with the excitonic transition at 40.4 meV. This phonon mode corresponds to ionic oscillation of the Janus layer only. In addition, strongly coupled  $E$  modes three and five (mostly the TMD layer moving) are both just 5 meV from the resonance. Therefore, our calculations predict that the IP-IL excitonic scattering mediated by optical phonons will be a particularly efficient process for the W-based HBL.

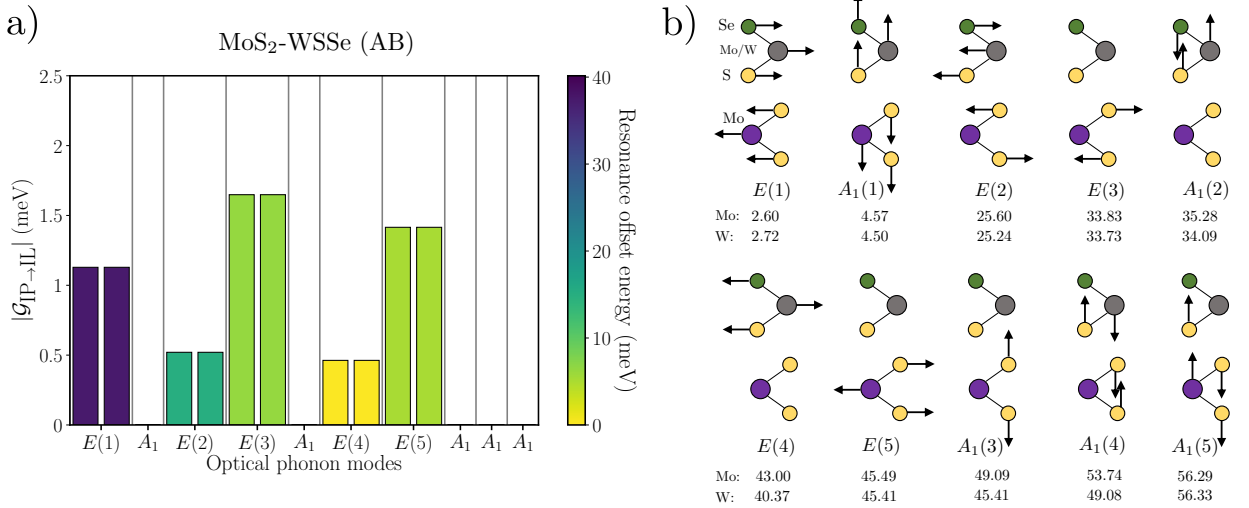


Figure 3: (a) Exciton-phonon coupling strengths,  $|G|$  (see Eq. (1)) for the intralayer (IP) to interlayer (IL) exciton scattering per phonon mode in MoS<sub>2</sub>@WSSe (AB stacking, see Fig. 2[d]). The colors report the resonance energy offset values (see text). (b) Oscillation patterns of the zone-center optical phonon modes for MoS<sub>2</sub>@MoSSe (AB stacking) and MoS<sub>2</sub>@WSSe (AB stacking). The arrow lengths are not scaled by the ionic masses, but they are set to zero for oscillations one order of magnitude weaker than the rest. The phonon energies associated with each mode are reported, in meV, for both systems.

## Conclusions

We have shown that the intrinsic net out-of-plane electric dipole moment of a Janus-type TMD layer has a strong influence on the optoelectronic properties of heterobilayer systems in which it is used. In particular, our first-principles analysis on  $\text{MoS}_2@\text{MoSSe}$ ,  $\text{MoS}_2@\text{MoSeS}$ ,  $\text{MoS}_2@\text{WSSe}$ , and  $\text{MoS}_2@\text{WSeS}$  demonstrates that the polarization direction of the Janus layer can be used to tune the dynamics of excitons – most notably by altering the energy separation between interlayer and in-plane excitonic states – without the use of external fields. Surprisingly, for  $\text{MoS}_2@\text{WSSe}$  the calculated energy difference is exactly resonant with in-plane optical phonon modes. Moreover, the calculated zero-momentum exciton-phonon couplings point to efficient in-plane to interlayer excitonic scattering mediated by optical phonons, again with  $\text{MoS}_2@\text{WSSe}$  being the prime candidate for this mechanism.

It is important to note, however, that this system also has an indirect band gap: hence, new low-lying dark excitonic states at finite momentum may be important, introducing an additional possible pathway for exciton dynamics which could be detrimental to the intra- to interlayer conversion rate. This opens a relevant future avenue of investigation theoretically, experimentally, and from a materials design perspective. Theoretically, the next step is computing the exciton-phonon couplings at finite momenta and simulating the excitonic relaxation dynamics in order to compare the transition rates of the various competing mechanisms. Experimentally, these quantities can be measured by photoluminescence and time-resolved, pump-and-probe studies. In materials design, it would be important to target excited-state properties both microscopically and at the excitonic level, rather than macroscopic optical properties at the single-particle level, in order to obtain candidate systems more effectively.

In conclusion, our results clearly support the use of Janus materials in layer engineering to boost the generation rate of long-lived interlayer excitons in heterobilayer TMD crystals. These excitons are obtained by phonon-assisted conversion of optically excited intralayer states.

# Methods

The single-particle wave functions and corresponding energies (DFT step) are obtained from density functional theory as implemented in the Quantum ESPRESSO code (QE)<sup>47</sup> using Perdew-Burke-Ernzerhof (PBE)<sup>65</sup> norm-conserving, fully relativistic pseudopotentials in the generalized gradient approximation (GGA)<sup>66</sup>. These were generated by the PseudoDojo project<sup>67</sup>. The plane-wave energy cutoff, vacuum separation between periodic repetitions of the simulation supercell, and  $k$ -grid sampling are, 120 Ry, 55 a.u. and  $42 \times 42 \times 1$  ( $\Gamma$  centered), respectively. We adopted Grimme’s dispersion correction (labeled as Grimme-D2 in QE)<sup>68,69</sup> in order to take van der Waals (vdW) interactions into account. The Many-Body Perturbation Theory calculations<sup>58</sup>, performed on top of the DFT results, were conducted with the YAMBO code.<sup>49,50</sup> The  $G_0W_0$ <sup>51,52</sup> corrections to the single-particle eigenvalues were computed with the plasmon-pole approximation for the dynamical electronic screening. The direct and indirect band gaps were converged with the  $42 \times 42 \times 1$   $k$ -grid mesh (yielding 169  $k$ -points in the irreducible Brillouin zone), summing over 600 and 900 states for the screening and the Green’s functions, respectively. The corrections were computed for the top 4 valence bands and the bottom 4 conduction bands. The BSE<sup>58</sup> for excitons was then solved in the Tamm-Dancoff approximation with RPA static screening, which was summed over 300 bands. The direct exciton energies and their wave functions were obtained for the first 12000 excitonic states by using the iterative scheme enabled by the SLEPC library.<sup>70</sup> The Coulomb cutoff (CC) technique was used along the out-of-plane direction to eliminate the long-ranged interactions with the repeated periodic images of the systems in both  $G_0W_0$  and BSE steps.<sup>53</sup> The same computational settings used at the DFT level, albeit with stricter convergence thresholds for the electronic wave functions, were adopted for the  $\Gamma$ -point calculation of phonon frequencies, eigenvector displacements and electron-phonon coupling matrix elements via Density Functional Perturbation Theory as implemented in the Quantum Espresso Code.<sup>48</sup> A dedicated Coulomb cutoff technique<sup>71</sup> was employed also in the phonon case.

## Supporting Information Available

Supplementary Information file includes the schematic representation of considered Janus HBLs, calculated band structures at both PBE and  $G_0W_0$  levels, and calculated  $\varepsilon_2$  with quasi-particle (via Bethe Salpeter Equation) and independent particle approximations.

## Acknowledgement

C. S. acknowledges funding by the the Air Force Office of Scientific Research (AFOSR, USA) under award number FA9550-19-1-7048. M. M acknowledges the Research Foundation-Flanders (FWO-Vlaanderen). F.P. acknowledges the European Union project: MaX *Materials design at the eXascale* H2020-INFRAEDI-2018-1, grant agreement n. 824143. L.W. acknowledges funding by the Fond National de Recherche, Luxembourg via project INTER/19/ANR/13376969/ACCEPT.

## References

- (1) He, K.; Kumar, N.; Zhao, L.; Wang, Z.; Mak, K. F.; Zhao, H.; Shan, J. Tightly Bound Excitons in Monolayer  $WSe_2$ . *Phys. Rev. Lett.* **2014**, *113*, 026803.
- (2) Mak, K. F.; Lee, C.; Hone, J.; Shan, J.; Heinz, T. F. Atomically Thin  $MoS_2$ : A New Direct-Gap Semiconductor. *Phys. Rev. Lett.* **2010**, *105*, 136805.
- (3) Splendiani, A.; Sun, L.; Zhang, Y.; Li, T.; Kim, J.; Chim, C.-Y.; Galli, G.; Wang, F. Emerging Photoluminescence in Monolayer  $MoS_2$ . *Nano Letters* **2010**, *10*, 1271–1275.
- (4) Das, S.; Robinson, J. A.; Dubey, M.; Terrones, H.; Terrones, M. Beyond Graphene: Progress in Novel Two-Dimensional Materials and van der Waals Solids. *Annual Review of Materials Research* **2015**, *45*, 1–27.

- (5) Molina-Sánchez, A.; Sangalli, D.; Hummer, K.; Marini, A.; Wirtz, L. Effect of spin-orbit interaction on the optical spectra of single-layer, double-layer, and bulk MoS<sub>2</sub>. *Phys. Rev. B* **2013**, *88*, 045412.
- (6) Qiu, D. Y.; da Jornada, F. H.; Louie, S. G. Optical Spectrum of MoS<sub>2</sub>: Many-Body Effects and Diversity of Exciton States. *Phys. Rev. Lett.* **2013**, *111*, 216805.
- (7) Chernikov, A.; Berkelbach, T. C.; Hill, H. M.; Rigosi, A.; Li, Y.; Aslan, O. B.; Reichman, D. R.; Hybertsen, M. S.; Heinz, T. F. Exciton Binding Energy and Nonhydrogenic Rydberg Series in Monolayer WS<sub>2</sub>. *Phys. Rev. Lett.* **2014**, *113*, 076802.
- (8) Wang, G.; Chernikov, A.; Glazov, M. M.; Heinz, T. F.; Marie, X.; Amand, T.; Urbaszek, B. Colloquium: Excitons in atomically thin transition metal dichalcogenides. *Rev. Mod. Phys.* **2018**, *90*, 021001.
- (9) Sidler, M.; Back, P.; Cotlet, O.; Srivastava, A.; Fink, T.; Kroner, M.; Demler, E.; Imamoglu, A. Fermi polaron-polaritons in charge-tunable atomically thin semiconductors. *Nature Physics* **2017-03**, *13*, 255 – 261.
- (10) Kogar, A.; Rak, M. S.; Vig, S.; Husain, A. A.; Flicker, F.; Joe, Y. I.; Venema, L.; MacDougall, G. J.; Chiang, T. C.; Fradkin, E.; van Wezel, J.; Abbamonte, P. Signatures of exciton condensation in a transition metal dichalcogenide. *Science* **2017**, *358*, 1314–1317.
- (11) Cotlet, O.; Zeytinoglu, S.; Sigrist, M.; Demler, E.; Imamoglu, A. Superconductivity and other collective phenomena in a hybrid Bose-Fermi mixture formed by a polariton condensate and an electron system in two dimensions. *Phys. Rev. B* **2016**, *93*, 054510.
- (12) Cui, Y.; Zhou, Z.; Li, T.; Wang, K.; Li, J.; Wei, Z. Versatile Crystal Structures and (Opto)electronic Applications of the 2D Metal Mono-, Di-, and Tri-Chalcogenide Nanosheets. *Advanced Functional Materials* **2019**, *29*, 1900040.



- (13) Wang, J.; Verzhbitskiy, I.; Eda, G. Electroluminescent Devices Based on 2D Semiconducting Transition Metal Dichalcogenides. *Advanced Materials* **2018**, *30*, 1802687.
- (14) Atatüre, M.; Englund, D.; Vamivakas, N.; Lee, S.-Y.; Wrachtrup, J. Material platforms for spin-based photonic quantum technologies. *Nature Reviews Materials* **2018**, *3*, 38–51.
- (15) Ross, J. S.; Klement, P.; Jones, A. M.; Ghimire, N. J.; Yan, J.; Mandrus, D. G.; Taniguchi, T.; Watanabe, K.; Kitamura, K.; Yao, W.; Cobden, D. H.; Xu, X. Electrically tunable excitonic light-emitting diodes based on monolayer WSe<sub>2</sub> p-n junctions. *Nature nanotechnology* **2014**, *9*, 268–272.
- (16) Baugher, B. W. H.; Churchill, H. O. H.; Yang, Y.; Jarillo-Herrero, P. Optoelectronic devices based on electrically tunable p-n diodes in a monolayer dichalcogenide. *Nature nanotechnology* **2014**, *9*, 262–267.
- (17) Jones, A. M.; Yu, H.; Ghimire, N. J.; Wu, S.; Aivazian, G.; Ross, J. S.; Zhao, B.; Yan, J.; Mandrus, D. G.; Xiao, D.; Yao, W.; Xu, X. Optical generation of excitonic valley coherence in monolayer WSe<sub>2</sub>. *Nature Nanotechnology* **2013**, *8*, 634–638.
- (18) Xiao, D.; Liu, G.-B.; Feng, W.; Xu, X.; Yao, W. Coupled Spin and Valley Physics in Monolayers of MoS<sub>2</sub> and Other Group-VI Dichalcogenides. *Phys. Rev. Lett.* **2012**, *108*, 196802.
- (19) Kang, J.; Tongay, S.; Zhou, J.; Li, J.; Wu, J. Band offsets and heterostructures of two-dimensional semiconductors. *Applied Physics Letters* **2013**, *102*, 012111.
- (20) Gillen, R.; Maultzsch, J. Interlayer excitons in MoSe<sub>2</sub>/WSe<sub>2</sub> heterostructures from first principles. *Phys. Rev. B* **2018**, *97*, 165306.
- (21) Deilmann, T.; Thygesen, K. S. Interlayer Excitons with Large Optical Amplitudes in Layered van der Waals Materials. *Nano Letters* **2018**, *18*, 2984–2989.

- (22) Torun, E.; Miranda, H. P. C.; Molina-Sánchez, A.; Wirtz, L. Interlayer and intralayer excitons in MoS<sub>2</sub>/WS<sub>2</sub> and MoSe<sub>2</sub>/WSe<sub>2</sub> heterobilayers. *Phys. Rev. B* **2018**, *97*, 245427.
- (23) Van der Donck, M.; Peeters, F. M. Interlayer excitons in transition metal dichalcogenide heterostructures. *Phys. Rev. B* **2018**, *98*, 115104.
- (24) Palummo, M.; Bernardi, M.; Grossman, J. C. Exciton Radiative Lifetimes in Two-Dimensional Transition Metal Dichalcogenides. *Nano Letters* **2015**, *15*, 2794–2800.
- (25) Robert, C.; Lagarde, D.; Cadiz, F.; Wang, G.; Lassagne, B.; Amand, T.; Balocchi, A.; Renucci, P.; Tongay, S.; Urbaszek, B.; Marie, X. Exciton radiative lifetime in transition metal dichalcogenide monolayers. *Phys. Rev. B* **2016**, *93*, 205423.
- (26) Chen, H.; Wen, X.; Zhang, J.; Wu, T.; Gong, Y.; Zhang, X.; Yuan, J.; Yi, C.; Lou, J.; Ajayan, P. M.; Zhuang, W.; Zhang, G.; Zheng, J. Ultrafast formation of interlayer hot excitons in atomically thin MoS<sub>2</sub>/WS<sub>2</sub> heterostructures. *Nature communications* **2016**, *7*, 12512–12512.
- (27) Kozawa, D.; Carvalho, A.; Verzhbitskiy, I.; Giustiniano, F.; Miyauchi, Y.; Mouri, S.; Castro Neto, A. H.; Matsuda, K.; Eda, G. Evidence for Fast Interlayer Energy Transfer in MoSe<sub>2</sub>/WS<sub>2</sub> Heterostructures. *Nano Letters* **2016**, *16*, 4087–4093.
- (28) Schaibley, J. R.; Yu, H.; Clark, G.; Rivera, P.; Ross, J. S.; Seyler, K. L.; Yao, W.; Xu, X. Valleytronics in 2D materials. *Nature Reviews Materials* **2016**, *1*, 16055.
- (29) Molina-Sánchez, A.; Sangalli, D.; Wirtz, L.; Marini, A. Ab Initio Calculations of Ultrashort Carrier Dynamics in Two-Dimensional Materials: Valley Depolarization in Single-Layer WSe<sub>2</sub>. *Nano Letters* **2017**, *17*, 4549–4555.
- (30) Ovesen, S.; Brem, S.; Linderälv, C.; Kuisma, M.; Korn, T.; Erhart, P.; Selig, M.;

- Malic, E. Interlayer exciton dynamics in van der Waals heterostructures. *Communications Physics* **2019**, *2*, 23.
- (31) Rivera, P.; Schaibley, J.; Jones, A.; Ross, J.; Wu, S.; Aivazian, G.; Klement, P.; Seyler, K.; Clark, G.; Ghimire, N.; Yan, J.; Mandrus, D.; Yao, W.; Xu, X. Observation of long-lived interlayer excitons in monolayer MoSe<sub>2</sub>-WSe<sub>2</sub> heterostructures. *Nature Communications* **2015**, *6*.
- (32) Montblanch, A. et al. Confinement of long-lived interlayer excitons in WS<sub>2</sub>/WSe<sub>2</sub> heterostructures. *Communications Physics* **2021**, *4*.
- (33) Fang, H. et al. Strong interlayer coupling in van der Waals heterostructures built from single-layer chalcogenides. *Proceedings of the National Academy of Science* **2014**, *111*, 6198–6202.
- (34) Heo, H.; Sung, J. H.; Cha, S.; Jang, B.-G.; Kim, J.-Y.; Jin, G.; Lee, D.; Ahn, J.-H.; Lee, M.-J.; Shim, J. H.; Choi, H.; Jo, M.-H. Interlayer orientation-dependent light absorption and emission in monolayer semiconductor stacks. *Nature Communications* **2015**, *6*, 7372.
- (35) Nayak, P. K.; Horbatenko, Y.; Ahn, S.; Kim, G.; Lee, J.-U.; Ma, K. Y.; Jang, A.-R.; Lim, H.; Kim, D.; Ryu, S.; Cheong, H.; Park, N.; Shin, H. S. Probing Evolution of Twist-Angle-Dependent Interlayer Excitons in MoSe<sub>2</sub>/WSe<sub>2</sub> van der Waals Heterostructures. *ACS Nano* **2017**, *11*, 4041–4050.
- (36) Gao, S.; Yang, L.; Spataru, C. D. Interlayer Coupling and Gate-Tunable Excitons in Transition Metal Dichalcogenide Heterostructures. *Nano Lett.* **2017**, *17*, 7809–7813.
- (37) Lu, A. K. A.; Houssa, M.; Luisier, M.; Pourtois, G. Impact of Layer Alignment on the Behavior of MoS<sub>2</sub>-ZrS<sub>2</sub> Tunnel Field-Effect Transistors: An Ab Initio Study. *Phys. Rev. Applied* **2017**, *8*, 034017.

- (38) Peimyoo, N.; Deilmann, T.; Withers, F.; Escolar, J.; Nutting, D.; Taniguchi, T.; Watanabe, K.; Taghizadeh, A.; Craciun, M. F.; Thygesen, K. S.; Russo, S. Electrical tuning of optically active interlayer excitons in bilayer MoS<sub>2</sub>. *Nature Nanotechnology* **2021**, *16*, 888–893.
- (39) Dong, L.; Lou, J.; Shenoy, V. B. Large In-Plane and Vertical Piezoelectricity in Janus Transition Metal Dichalcogenides. *ACS Nano* **2017**, *11*, 8242–8248.
- (40) Qin, Y.; Sayyad, M.; Montblanch, A. R.-P.; Feuer, M. S. G.; Dey, D.; Blei, M.; Sailus, R.; Kara, D. M.; Shen, Y.; Yang, S.; Botana, A. S.; Atature, M.; Tongay, S. Reaching the Excitonic Limit in 2D Janus Monolayers by In Situ Deterministic Growth. *Advanced Materials* **2022**, *34*, 2106222.
- (41) Zhang, X.; Pang, R.; Hou, X.; Wang, S. Stacking-tailoring quasiparticle energies and interlayer excitons in bilayer Janus MoSSe. *New Journal of Physics* **2021**, *23*, 013003.
- (42) Trivedi, D. B. et al. Room-Temperature Synthesis of 2D Janus Crystals and their Heterostructures. *Advanced Materials* **2020**, *32*, 2006320.
- (43) Li, F.; Wei, W.; Huang, B.; Dai, Y. Excited-State Properties of Janus Transition-Metal Dichalcogenides. *The Journal of Physical Chemistry C* **2020**, *124*, 1667–1673.
- (44) Peng, R.; Ma, Y.; Zhang, S.; Huang, B.; Dai, Y. Valley Polarization in Janus Single-Layer MoSSe via Magnetic Doping. *The Journal of Physical Chemistry Letters* **2018**, *9*, 3612–3617.
- (45) Jin, C.; Tang, X.; Tan, X.; Smith, S. C.; Dai, Y.; Kou, L. A Janus MoSSe monolayer: a superior and strain-sensitive gas sensing material. *J. Mater. Chem. A* **2019**, *7*, 1099–1106.
- (46) Li, L.; Li, B.; Guo, Q.; Li, B. Theoretical Screening of Single-Atom-Embedded MoSSe

- Nanosheets for Electrocatalytic N<sub>2</sub> Fixation. *The Journal of Physical Chemistry C* **2019**, *123*, 14501–14507.
- (47) Giannozzi, P.; Baseggio, O.; Bonfà, P.; Brunato, D.; Car, R.; Carnimeo, I.; Cavazzoni, C.; de Gironcoli, S.; Delugas, P.; Ferrari Ruffino, F.; Ferretti, A.; Marzari, N.; Timrov, I.; Urru, A.; Baroni, S. Quantum ESPRESSO toward the exascale. *The Journal of Chemical Physics* **2020**, *152*, 154105.
- (48) Baroni, S.; de Gironcoli, S.; Dal Corso, A.; Giannozzi, P. Phonons and related crystal properties from density-functional perturbation theory. *Rev. Mod. Phys.* **2001**, *73*, 515–562.
- (49) Marini, A.; Hogan, C.; Grüning, M.; Varsano, D. yambo: An ab initio tool for excited state calculations. *Computer Physics Communications* **2009**, *180*, 1392–1403.
- (50) Sangalli, D. et al. Many-body perturbation theory calculations using the yambo code. *Journal of Physics: Condensed Matter* **2019**, *31*, 325902.
- (51) Hedin, L.; Lundqvist, S. In *Effects of Electron-Electron and Electron-Phonon Interactions on the One-Electron States of Solids*; Seitz, F., Turnbull, D., Ehrenreich, H., Eds.; Solid State Physics; Academic Press, 1970; Vol. 23; pp 1–181.
- (52) Onida, G.; Reining, L.; Rubio, A. Electronic excitations: density-functional versus many-body Green’s-function approaches. *Rev. Mod. Phys.* **2002**, *74*, 601–659.
- (53) Ismail-Beigi, S. Truncation of periodic image interactions for confined systems. *Phys. Rev. B* **2006**, *73*, 233103.
- (54) Cudazzo, P. First-principles description of the exciton-phonon interaction: A cumulant approach. *Phys. Rev. B* **2020**, *102*, 045136.
- (55) Kandemir, A.; Sahin, H. Bilayers of Janus WSSe: monitoring the stacking type via the vibrational spectrum. *Phys. Chem. Chem. Phys.* **2018**, *20*, 17380–17386.

- (56) Yin, W.-J.; Wen, B.; Nie, G.-Z.; Wei, X.-L.; Liu, L.-M. Tunable dipole and carrier mobility for a few layer Janus MoSSe structure. *J. Mater. Chem. C* **2018**, *6*, 1693–1700.
- (57) URL\_will\_be\_inserted\_by\_publisher, See Supplementary Materials for Structural and Electronic properties of all the considered materials in this study.
- (58) Martin, R. M.; Reining, L.; Ceperley, D. M. *Interacting electrons – Theory and Computational Approaches*; Cambridge University Press, 2016.
- (59) Chen, H.-Y.; Bernardi, M. First-Principles Ultrafast Exciton Dynamics and Time-Domain Spectroscopies: Dark-Exciton Mediated Valley Depolarization in Monolayer WSe<sub>2</sub>. 2022; <https://arxiv.org/abs/2210.05964>.
- (60) Reichardt, S.; Wirtz, L. Nonadiabatic exciton-phonon coupling in Raman spectroscopy of layered materials. *Sci. Adv.* **2020**, *6*, eabb5915.
- (61) Chen, H.-Y.; Sangalli, D.; Bernardi, M. Exciton-Phonon Interaction and Relaxation Times from First Principles. *Phys. Rev. Lett.* **2020**, *125*, 107401.
- (62) Antonius, G.; Louie, S. G. Theory of exciton-phonon coupling. *Phys. Rev. B* **2022**, *105*, 085111.
- (63) Paleari, F.; Marini, A. Exciton-phonon interaction calls for a revision of the “exciton” concept. *Phys. Rev. B* **2022**, *106*, 125403.
- (64) Molina-Sánchez, A.; Hummer, K.; Wirtz, L. Vibrational and optical properties of MoS<sub>2</sub>: From monolayer to bulk. *Surface Science Reports* **2015**, *70*, 554–586.
- (65) Perdew, J. P.; Burke, K.; Ernzerhof, M. Generalized Gradient Approximation Made Simple. *Phys. Rev. Lett.* **1996**, *77*, 3865–3868.
- (66) Hamann, D. R. Optimized norm-conserving Vanderbilt pseudopotentials. *Phys. Rev. B* **2013**, *88*, 085117.

- (67) van Setten, M.; Giantomassi, M.; Bousquet, E.; Verstraete, M.; Hamann, D.; Gonze, X.; Rignanese, G.-M. The PseudoDojo: Training and grading a 85 element optimized norm-conserving pseudopotential table. *Computer Physics Communications* **2018**, *226*, 39–54.
- (68) Grimme, S. Semiempirical GGA-type density functional constructed with a long-range dispersion correction. *Journal of Computational Chemistry* **2006**, *27*, 1787–1799.
- (69) Barone, V.; Casarin, M.; Forrer, D.; Pavone, M.; Sami, M.; Vittadini, A. Role and effective treatment of dispersive forces in materials: Polyethylene and graphite crystals as test cases. *Journal of Computational Chemistry* **2009**, *30*, 934–939.
- (70) Hernandez, V.; Roman, J. E.; Vidal, V. SLEPc: A Scalable and Flexible Toolkit for the Solution of Eigenvalue Problems. *ACM Trans. Math. Softw.* **2005**, *31*, 351–362.
- (71) Sohler, T.; Calandra, M.; Mauri, F. Density functional perturbation theory for gated two-dimensional heterostructures: Theoretical developments and application to flexural phonons in graphene. *Phys. Rev. B* **2017**, *96*, 075448.